Comparison of Inviscid Flow Computations with Flight Data for the Shuttle Orbiter

K. James Weilmuenster*
NASA Langley Research Center, Hampton, Virginia

A three-dimensional inviscid flowfield code (HALIS) has been run for a nearly complete Shuttle vehicle for $6.0 \le M_\infty \le 21.6$ and $26.6 \text{ deg} \le \alpha \le 40$ deg. Both perfect gas and effective gamma HALIS solutions have been compared with four points along the STS-3 reentry trajectory and two points on the STS-5 reentry trajectory. In general, the HALIS results have agreed very well with the flight data. At high Mach numbers, the excellent agreement of flight data and effective gamma flowfield solutions shows that gamma has a significant effect on the Shuttle's wing windward surface pressure distributions. HALIS solutions also indicate that centerline pressure distributions at the aft end of the Shuttle vehicle are altered by gamma effects. A comparison of flight data and computed solutions in this region was inconclusive due to a lack of flight data density and flight-to-flight data scatter. In addition, HALIS results have been used to illustrate the effects of Mach number and angle of attack on the large-scale shock structure about the Shuttle vehicle as well as a detailed view of the bow shock/wing shock interaction region.

Introduction

RECENT advances in computational techniques and computer hardware have made it possible to attack the problem of computing steady-state inviscid flowfields over complex three-dimensional bodies such as the Space Shuttle Orbiter. These inviscid solutions provide the surface pressure distribution necessary to determine aerodynamic loads as well as other flow properties needed to compute surface heating rates.[1]

Vehicles such as the Shuttle Orbiter operate over a wide range of angle of attack and Mach number when entering the Earth's atmosphere. As shown in Fig. 1, the entry trajectory is characterized by flight at a moderate angle of attack ($\alpha < 30$ deg) and flight at a high angle of attack ($\alpha > 30$ deg). At moderate angles of attack, the subsonic portion of the flowfield is confined to the area about the vehicle nose cap. For some time there have been a number of techniques[2-4] available for computing solutions for these moderate angles of attack. These techniques take advantage of the small region of subsonic flow in the nose region where initial data surfaces can be obtained to initiate spatial marching methods for that portion of the flow over the vehicle which is supersonic. However, such methods fail at high angles of attack when subsonic flow can extend over a large portion of the vehicle windward surface.

A time-asymptotic computational code, called HALIS, has been developed to handle the high-angle-of-attack problem for the inviscid flow over the Space Shuttle and similar vehicles. The results of high-angle-of-attack flowfield computations generated over these vehicles by the HALIS code is presented in Refs. 5 and 6. In Ref. 6, this code was modified to include all of the Shuttle vehicle forward of the wing root. Also, a real gas computation capability was added to the code. In Ref. 6, body surface pressures generated by the HALIS code were shown to be in excellent agreement with flight pressures measured on the Shuttle vehicle.

In this present work, results from the HALIS code, which has been extended to cover the first 1212 in. of the Shuttle vehicle (approximately 93% of the total vehicle length), will be compared with flight surface pressures. Also, shock shapes at two angles of attack will be presented along with an analysis of the extent and strength of the internal wing shock.

Overview of the HALIS Code

The methodology behind and structure of the HALIS code is presented in detail in Ref. 7. Briefly, the code is a time-asymptotic solution of the Euler equations which utilizes an unsplit MacCormack differencing scheme. The solution space is the volume between the body surface and the bow shock wave, which is treated as a time-dependent boundary condition. This leads to a coordinate system defined by the position of the bow shock and body as well as the spatial derivatives along these surfaces. A spherical coordinate system is used to describe the blunt nose cap region of the flowfield, while a cylindrical coordinate system is used to describe the rest of the flowfield. The physical coordinate system is illustrated in Fig. 2a by a symmetry plane view and in Fig. 2b by a cross-sectional plane view, where for clarity a number of grid lines have been removed from each figure.

The HALIS code is written for use on the CDC Cyber 203, a vector processor, which has an incore memory of 10^6 64-bit words. In the solutions of Ref. 6, defining the first half of the Shuttle flowfield with a reasonable degree of resolution required the entire 10^6 words of memory. In order to expand the code to encompass the first 1212 in. of the Shuttle vehicle, it was necessary to rewrite the code in the SL/1 language (a vector language developed at NASA Langley Research Center to allow half-word arithmetic operations on the CYBER 203). This revision then doubled the available memory and essentially allowed a doubling of the flowfield that could be covered.

The Shuttle vehicle has a total length measured from nose to body-flap hinge line of 1293 in. The HALIS code is limited

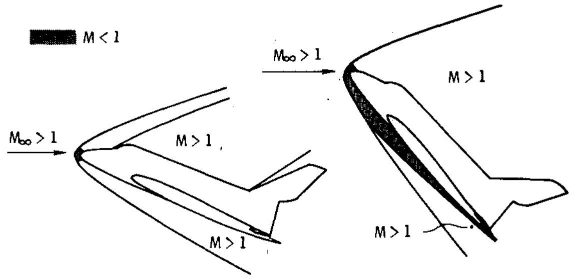

Fig. 1 External flowfields, supersonic/hypersonic flight regime.

Presented as Paper 83-1798 at the AIAA Applied Aerodynamics Conference, Danvers, Mass., July 13-15, 1983; submitted July 21, 1983; revision received March 5, 1984. This paper is declared a work of the U.S. Government and therefore is in the public domain.

*Aerospace Technologist, Aerothermodynamics Branch, Space Systems Division. Member AIAA.

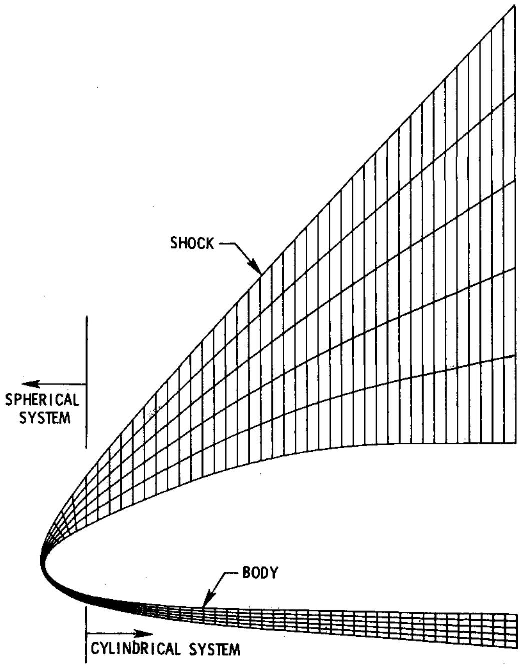

Fig. 2a Physical grid, symmetry plane.

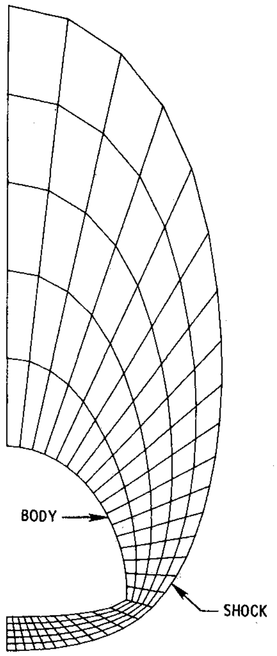

Fig. 2b Physical grid, cross flow plane.

to modeling the first 1212 in. of the vehicle since the coordinate transformations used in the code are not capable of handling the geometry at the extreme aft end of the vehicle. All previous work with the code had, with good results, used equal increments in the angular coordinate in the cross-flow plane. However, initial computations using a fully winged vehicle indicated a lack of resolution of the flowfield about the wing tips. To remedy this problem, a second transformation of the angular coordinate was made which generated a greater density of grid points in the region of the wing tip. In Fig. 3, the resulting vehicle geometry used in the following computations is shown. As in previous work, the upper surface of the wing (a region dominated by viscous effects) has been filled in with an elliptic-curve segment which eliminates the need to deal with the vehicle's complex leeside geometry. QUICK,[8] a rapid-response geometry code, has been used to define the vehicle surface and to generate the necessary surface derivatives used in the coordinate transformations.

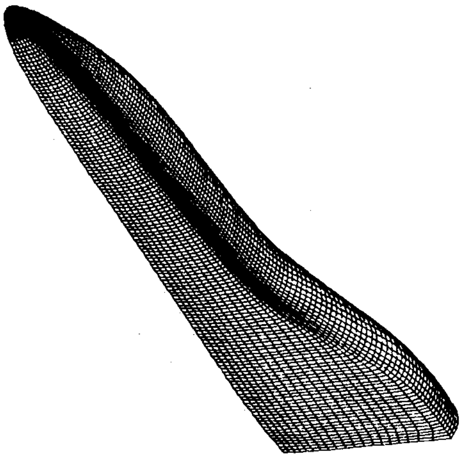

(a) LOWER SURFACE.

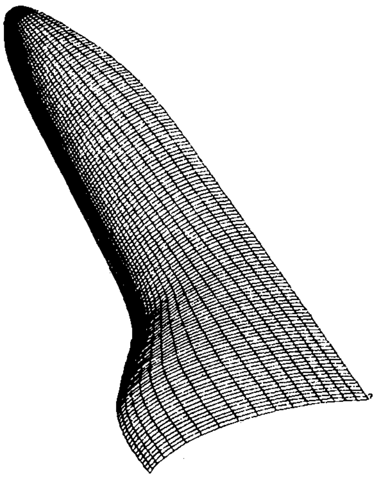

(b) UPPER SURFACE.

Fig. 3 Complete Shuttle Orbiter geometry with modified lee surface.

For the results presented in this paper, the HALIS code has been configured in the following manner. There are a total of 145 planes down the vehicle, 15 in the spherical coordinate system, and 130 in the cylindrical coordinate system. There are 39 planes around the body which include two rays of information reflected across the upper and lower symmetry planes, and there are 15 points located along each ray between the body and bow shock wave. The result is a flowfield containing 84,825 grid points. This number of grid points, when translated into a working code, fills all of the available 2×10^6 half-word CPU storage on the Cyber 203. This, the author feels, represents a minimum in the number of grid points needed to generate a reliable solution. In fact, the grid used was not sufficient to resolve some very large normal entropy gradients which occurred at the surface near the wing tips. For this reason, the constant entropy wall boundary condition was not enforced in the solutions presented later in this paper. Since surface pressures are of interest here, the solutions are still valid, regardless of the surface entropy boundary condition, as demonstrated in Ref. 7.

In general, the HALIS code produced converged solutions in approximately 1200 global iterations, which translates into 90 min of CPU time, with the low-angle-of-attack cases requiring fewer iterations to convergence than the high-angle-of-attack cases.

Because of the large number of grid points required to provide adequate resolution in the flowfield, the equilibrium air chemistry routine was removed from the code to free space in the CPU. Thus, any real-gas computations made using the full vehicle configuration will have to simulate real-gas effects through the use of an effective gamma. The accuracy of effective gamma calculations in modeling real-gas pressures was shown in Ref. 7.

Shuttle Flight Data System

Through its first five flights the Space Shuttle Orbiter has been fitted with a data acquisition system to record the surface pressures and temperatures on the vehicle through both the ascent and descent phases of its flights. The DFI (Development Flight Instrumentation) system consists of a matrix of sensors covering the surface of the vehicle. The locations of the windward surface pressure sensors of interest in this paper are shown on Fig. 4. These pressure transducers were in general sized for the pressure levels expected during the peak heating phase of the reentry trajectory which have limited the availability of some of the pressure data during the latter portion of the reentry. There is one 15-psia transducer located on the nose cap; this is denoted by a filled symbol in Fig. 4. Also, a 150-psf transducer is colocated at this position. The half-filled symbols represent 150-psf transducers; the open symbols represent 75-psf transducers. In general, the 15-psia and 150-psf transducers provide pressure data through the entire reentry over the range of Mach number and angle of attack of interest in this paper ($M_\infty = 6$ and above and $\alpha = 25$ to 45 deg) while the data from the 75-psf gauges are, with some exceptions, only available for $M_\infty > 15$. Because of system problems, the only complete sets of pressure data are from the third (STS-3) and fifth (STS-5) Shuttle flights, and it is these data bases which are used in this paper, although partial pressure data bases exist for STS-1 and STS-4. In Fig. 4, the vehicle surface aft of the dashed line between wing tips was instrumented. However, as mentioned before, the HALIS computations were limited to the vehicle forward of the dashed line. Also, in Fig. 4, the heavy solid line labeled elevon hinge line is shown. All computations used in this paper were made with a zero deflection of the elevons which is a deviation from actual flight conditions.

The reduction and analysis of the flight pressure data used in this paper follow the procedures outlined in Ref. 9. There are, of course, many possibilities for error to appear in the flight data due to instrumentation limitations and data-reduction procedures. The flight data presented here have been corrected where possible for any apparent bias or calibration errors.

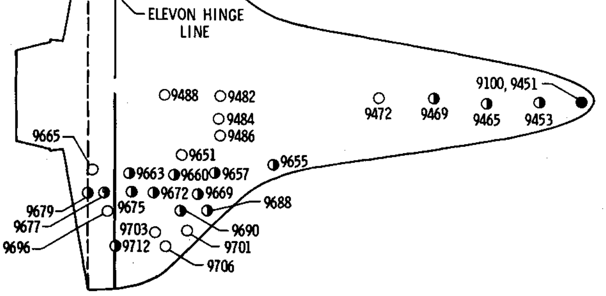

Fig. 4 Windward surface pressure port locations.

Table 1 Flight surface pressure time history plots

Symbol	Mach No.	Angle of attack, deg
○	6.00	26.6
□	10.00	38.4
◇	16.25	39.8
△	21.60	40.0

HALIS/Flight Data/Tunnel Data Comparison

HALIS computations have been made for four points on the STS-3 reentry trajectory. The flight points used and their identifying symbols, which will appear on the following plots of flight surface pressure time histories, are listed in Table 1. The 6.00 and 10.00 Mach number cases were run using a ratio of specific heats γ of 1.4. The $M_\infty = 16.25$ case was computed using a $\gamma = 1.4$ and an effective gamma, $\gamma_e = 1.2$, while the $M_\infty = 21.6$ case was run with a $\gamma = 1.4$ and a $\gamma_e = 1.18$. The effective gamma used in these calculations is taken to be the gamma required to produce the real-gas density ratio across a conical shock having a half-angle equal to the body deflection angle of the orbiter vehicle along the flat windward surface. In addition, wind-tunnel tests of a Shuttle pressure model in the NASA Langley Research Center Continuous Flow Hypersonic Tunnel (CFHT)[10] were made at the Mach $M_\infty = 10$ flight point, and a comparison of tunnel data, flight data and HALIS computations will be made at this flight condition.

In Ref. 6, a thorough analysis of flow over the forward windward surface of the Shuttle was made along with comparisons to flight data. Thus, in this paper, only centerline pressures and pressures from points located aft of the wing root will be presented. Figures 5a-5d are plots of flight and HALIS pressures plotted against time for the windward surface pressure sensors whose locations are indicated on Fig. 4. The $M_\infty = 16.25$ and $M_\infty = 21.6$ HALIS results shown on these plots were obtained using the respective effective gamma for each case.

On all plots the pressure has been nondimensionalized by the freestream dynamic pressure Q. All of the pressure plots have characteristics similar to those found on Fig. 5a, pressure port 9100. The first useable pressures begin at approximately 56,400 s Greenwich Mean Time (GMT). The long, flat pressure region is the high Mach number portion of the trajectory and is flown at a constant angle of attack (40 deg). This part of the trajectory is terminated by a pullup, pushover vehicle maneuver at 57,000 s GMT. During this maneuver the vehicle attains its highest angle of attack (43.2 deg). From this point on, Mach number and angle of attack decrease monotonically through the trajectory until a P/Q minimum is reached at approximately 57,500 s, which is about $M_\infty = 4$ in the reentry trajectory. Figure 5b shows the pressure time history of the 150 psf sensor 9451 colocated with sensor 9100, which, due to the higher resolution, provides a smooth trace of the pressure over the early portion of the trajectory.

In general, the HALIS results and flight data are in good to excellent agreement as indicated by the comparison of flight and computed pressures at the location of the pressure port 9660 (Fig. 5c). Notable exceptions to this agreement are ports 9665, 9677, 9679, 9696, and 9712 (Fig. 5g), which lie on or at the edge of the elevons. For these ports, the flight pressure is considerably higher than the HALIS predictions, as illustrated by Fig. 5d, which is not surprising, since over this portion of the trajectory the elevons are set at a positive deflection (into the stream) forming a compression surface.

For three of the four HALIS solutions corresponding to the selected entry trajectory conditions, a comparison of HALIS and flight pressures along the windward surface centerline as well as chordwise pressures at semispan locations of 0.4, 0.5, 0.6, 0.7, and 0.8 will be presented in the following figures.

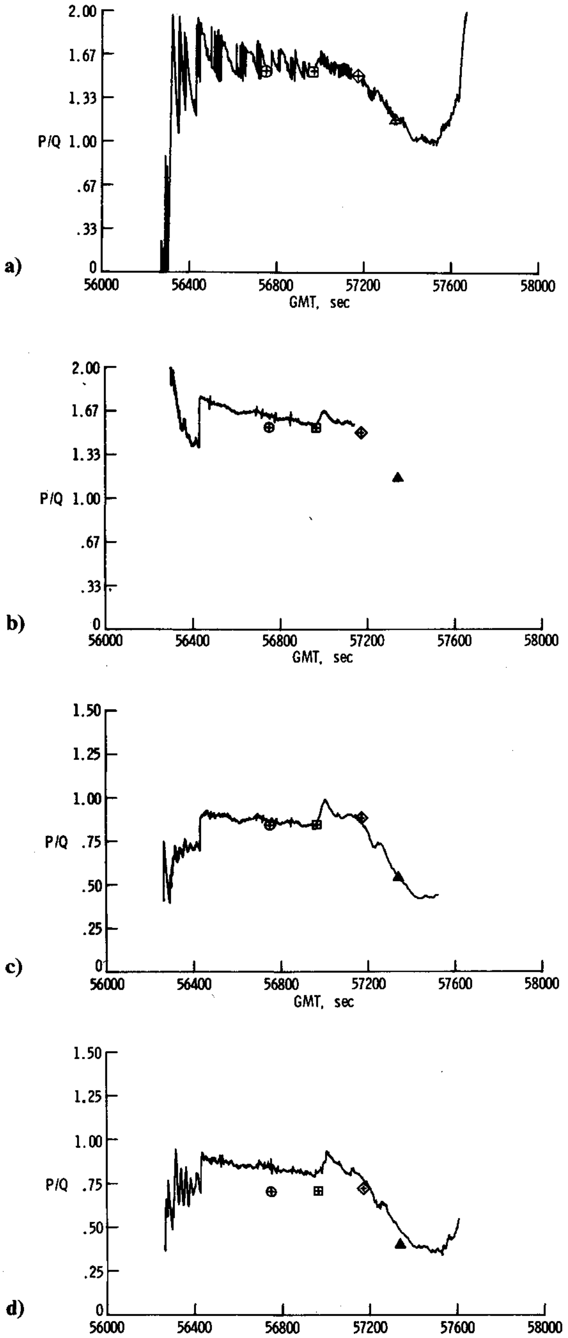

Fig. 5 Comparison of flight data with HALIS results: a) pressure port 9100; b) pressure port 9451; c) pressure port 9660; d) pressure port 9677.

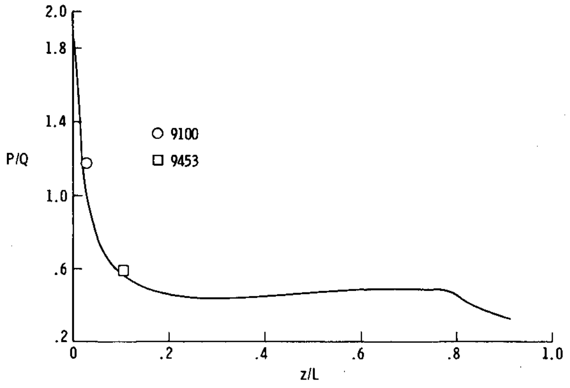

Fig. 6 Comparison of HALIS/flight centerline pressures, $M_\infty = 6.0$, $\alpha = 26.6$ deg, $\gamma = 1.4$.

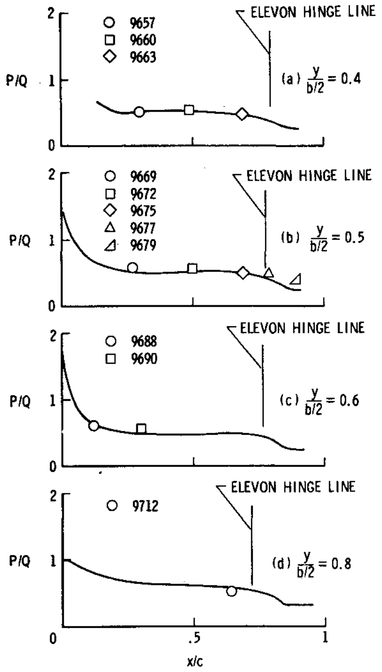

Fig. 7 Comparison of HALIS/flight chordwise pressure distributions at semispan locations of 0.4, 0.5, 0.6, and 0.8; $M_\infty = 6.0$, $\alpha = 26.6$ deg, $\gamma = 1.4$.

For the $M_\infty = 6.0$ case, the available flight data are limited by transducer saturation. Figure 6 shows the centerline pressure a function of nondimensional vehicle length, Z/L, where the vehicle length, L, is taken to be 1293 in., the distance from the nose to the body flap hinge line. Its shape is typical regardless of Mach number or angle of attack, with the large drop in pressure with increasing distance from the stagnation point, a weak recompression, and a large expansion at the aft end of the vehicle caused by the surface geometry. The two flight data points agree very well with the HALIS results. Figures 7a-7d show comparisons of computed results and flight pressures as a function of nondimensional chord length for the semispan locations of 0.4, 0.5, 0.6, and 0.8. Note in Fig. 7b that the two pressure ports located aft of the elevon hinge line reflect the flight condition of an elevon deflected into the stream.

Results from tests of a 0.006-scale model done by Charles G. Miller III in the Langley CFHT tunnel at the $M_\infty = 10$ flight condition[10] have been compared with HALIS results as well as flight data. In Fig. 8, tunnel and flight data are compared to the HALIS solution for the centerline pressure distribution with good agreement between all three data sources. Figure 9, a plot of pressure against nondimensional span, again compares tunnel, flight, and HALIS pressures at a Z/L of 0.8 for a full-scale span of 430.5 in. The HALIS results and tunnel data are in excellent agreement up to a span of 0.7. Beyond 0.7 the tunnel data do not follow the pressure drop in the HALIS solution. This pressure drop could be a purely numerical response to the large pressure gradient at the wing leading edge, since there are only seven grid points between the 0.7 span location and the leading edge. However, the same type of pressure distributions have been noted in solutions generated by the STEIN[2] code when computing the flow over similar configurations. Also, although no computations have been made with a higher grid density in the vicinity of the leading edge, solutions generated with a reduced grid density in this region do not indicate an appreciable change in

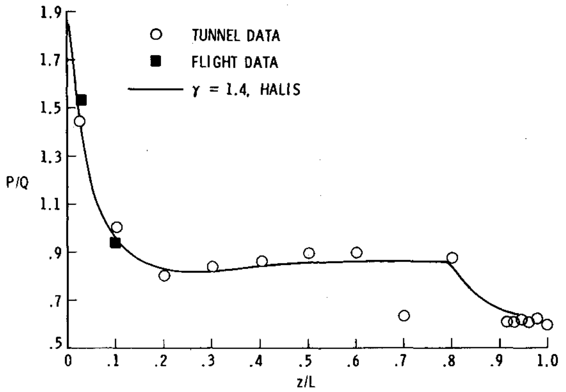

Fig. 8 Comparison of HALIS/flight/tunnel centerline pressures; $M_\infty = 10.0$, $\alpha = 38.4$ deg, and $\gamma = 1.4$.

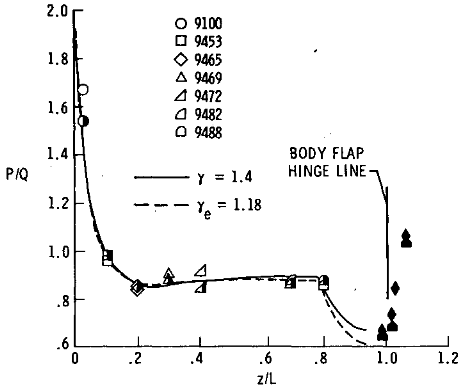

Fig. 11 Comparison of HALIS/flight centerline pressures; $M_\infty = 21.6$, $\alpha = 40$ deg for $\gamma = 1.4$ and $\gamma_e = 1.18$.

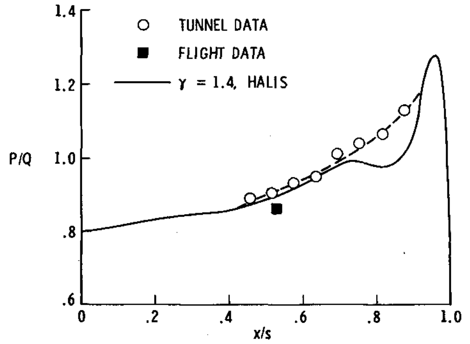

Fig. 9 Comparison of HALIS/flight/tunnel spanwise pressure distributions at a $Z/L = 0.8$; $M_\infty = 10.0$, $\alpha = 38.4$ deg, and $\gamma = 1.4$.

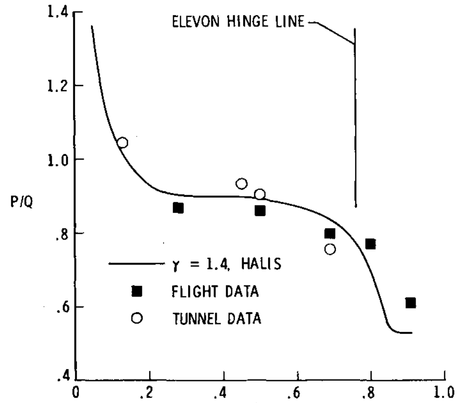

Fig. 10 Comparison of HALIS/flight/tunnel chordwise pressure distributions at a semispan location of 0.5; $M_\infty = 10.0$, $\alpha = 38.4$ deg, and $\gamma = 1.4$.

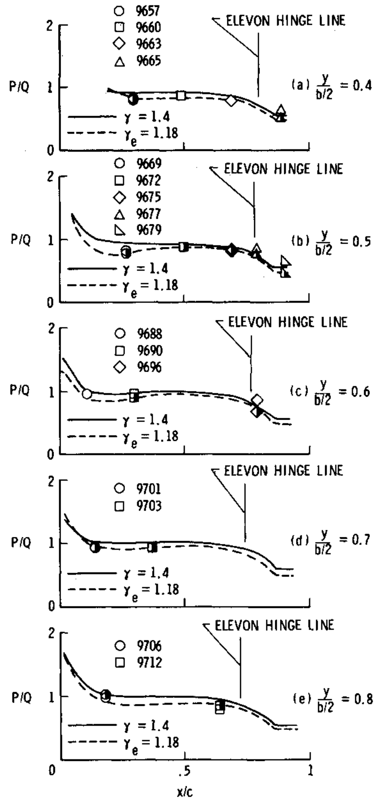

Fig. 12 Comparison of HALIS/flight chordwise pressure distributions at semispan locations of 0.4, 0.5, 0.6, 0.7, and 0.8; $M_\infty = 21.6$, $\alpha = 40$ deg for $\gamma = 1.4$, and $\gamma_e = 1.18$.

the pressure distribution as indicated in Fig. 9. The one flight data point available agrees very well with the HALIS results and tunnel data. A distribution of HALIS, flight and tunnel pressures as a function of non-dimensional chord length, x/c, at the 0.5 span are compared in Fig. 10. Again, except for the tunnel pressure at $x/c = 0.69$, there is very good agreement between the three data sources. As before, the elevated flight pressures aft of the elevon hinge line are due to elevon deflection.

The last flight data point, $M_\infty = 21.6$, was chosen because the STS-3 and STS-5 entry trajectories were coincident at this point, thus providing two sets of flight data for each computed flight point. At these high Mach numbers, real-gas effects become important. Thus, for each flight point both a perfect gas and an effective gamma HALIS solution have been computed for comparison with the flight data. For these figures, the open symbols represent STS-3 data and half-filled symbols represent STS-5 data.

The centerline pressure distribution for the $M_\infty = 21.6$ flight point is shown in Fig. 11, where both the perfect gas and effective gamma HALIS solutions have been plotted along with the STS-3 and STS-5 flight points. The two HALIS solutions are similar up to a Z/L of 0.5, except for the stagnation region which is poorly detailed in this figure (for detailed plots of pressure distributions in the stagnation region, see Ref. 6). However, for $Z/L > 0.5$, the $\gamma_e = 1.18$ solution produces a lower pressure level along the centerline with the greatest effect occurring in the expansion region on the aft end of the vehicle. The computed solutions are in good

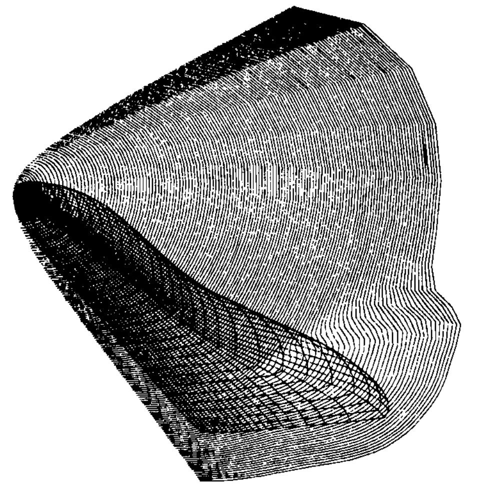

(a) LOWER SURFACE.

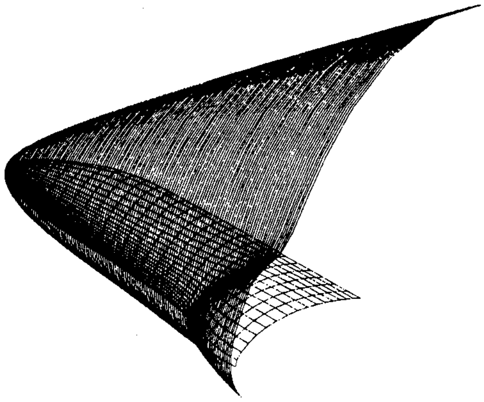

(b) UPPER SURFACE.

Fig. 13 External shock structure, $M_\infty = 6.0$, $\alpha = 26.6$ deg, $\gamma = 1.4$.

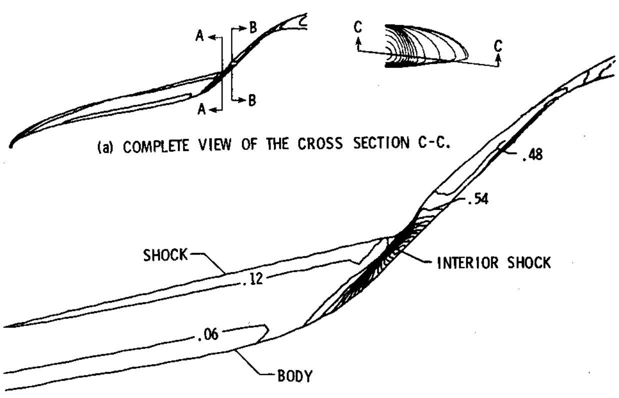

(b) EXPANDED VIEW OF SHOCK INTERACTION REGION.

Fig. 14 Body shock/wing shock interaction, nondimensional pressure contours, $M_\infty = 6.0$, $\alpha = 26.6°$, $\gamma = 1.4$.

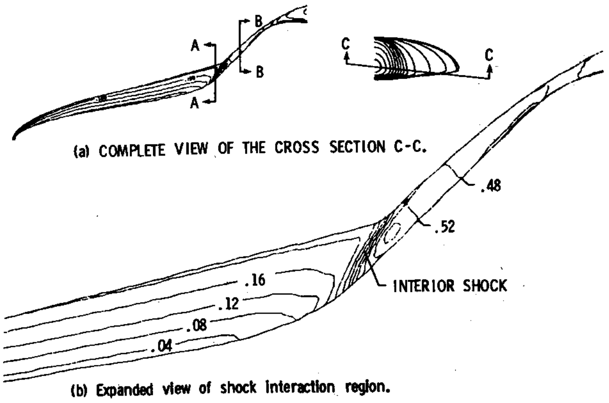

(b) Expanded view of shock interaction region.

Fig. 15 Body shock/wing shock interaction, nondimensional pressure contours, $M_\infty = 16.25$, $\alpha = 39.8$ deg, $\gamma = 1.4$.

agreement with the flight data. At this Mach number, surface pressure sensors located on the centerline just upstream of and on the body flap are not yet saturated. These pressures have also been plotted on Fig. 11. STS-3 pressures tend to confirm the gamma effect on the pressure distribution over the aft body expansion while the STS-5 pressures agree better with the perfect-gas solution. In Figs. 12a-12e, the chordwise pressure distributions are compared with the flight data at spanwise locations of 0.4, 0.5, 0.6, 0.7, and 0.8. In all of these figures it can be seen that real-gas effects have a large impact on the pressure distributions over the wing surface, and the flight data strongly support the results of the effective gamma HALIS solution. At this flight condition, the STS-3 elevon deflection is approximately 5 deg while the deflection is only 2 deg for STS-5.

Shock Geometry

The geometry of the shock envelope about the Shuttle vehicle is of interest because of speculation that the location and strength of the wing shock/body shock interaction may be part of the process which creates the "streak heating"[11] seen on the windward surface of the Shuttle wings.

From HALIS results, three-dimensional perspective views of the shock surface surrounding the Shuttle vehicle and superimposed on the vehicle have been created. Two such perspective views are shown on Fig. 13 for the STS-3 flight data point of $M_\infty = 6.0$ and an angle of attack of 26.6 deg. In Fig. 13a, a view from in front and below the vehicle, the complete shock envelope can be seen. It is also possible to see the region where the bow shock and the external wing shock intersect. A perspective view from above and behind shown in Fig. 13b provides a better view of the bow shock/external wing shock interaction.

Figure 13 gives a view of the large-scale shock structure. A more detailed view may be obtained by looking at Fig. 14. Figure 14a is a contour plot of nondimensional pressure in the z-r plane of data bounded above by the shock and below by the body and lying in the cross-section C-C. At this flight condition, $M_\infty = 6$, Fig. 14a clearly defines the point at which the bow shock and exterior wing shock interact. Because the HALIS code integrates the conservative form of the Euler equations, shocks which lie within the computational domain are captured. In Fig. 14b, a blowup of a portion of Fig. 14a clearly shows the interior wing shock as the tight pressure gradient (represented by the high concentration of contour lines) which extends toward the wing root. For the flight point $M_\infty = 16.25$, $\alpha = 39.8$ deg, Fig. 15a shows the nondimensional pressure contour plots in the cross section C-C. For the $\alpha = 39.8$ deg case, the bow shock/exterior wing shock interaction occurs at about the same axial location as for the $\alpha = 26.6$ deg case, but at a point approximately twice the distance from the body surface as the previous case. Also, as indicated by Fig. 15b, the interior wing shock is much weaker than that in the $\alpha = 26.6$ deg case.

Since HALIS is an inviscid code, it would be inappropriate to use HALIS results to make any inference about surface heating. However, in light of the above analysis of the external shock structure, it is worthwhile to note those areas where the HALIS results support the basic findings about the "streak heating" phenomenon as presented in Ref. 11. Namely, the streaks seem to originate at a point near the wing/body shock intersection, and the severity of the heating decreases with increasing angle of attack, which corresponds to a decreased strength of the interior wing shock as determined by the HALIS code.

Concluding Remarks

The HALIS code has been run for a nearly complete Shuttle vehicle for $6.0 < M_\infty < 21.6$ and $26.6 \text{ deg} < \alpha < 40$ deg. Both perfect-gas and effective gamma HALIS solutions have been compared with four points along the STS-3 reentry trajectory and two points on the STS-5 reentry trajectory. In general, the HALIS results have agreed very well with the flight data. At high Mach numbers, the excellent agreement of flight data and effective gamma solutions shows that real-gas effects have a significant effect on the Shuttle's wing, windward surface pressure distributions. HALIS solutions also indicate that centerline pressure distributions at the aft end of the Shuttle vehicle are altered by real-gas effects. A comparison of flight data and computed solutions in this region were inconclusive due to a lack of flight data density and flight-to-flight data scatter. In addition, HALIS results have been used to illustrate the effect of Mach number and angle of attack on the large-scale shock structure about the Shuttle vehicle as well as a detailed view of the bow shock/wing shock interaction region.

References

[1] Hamilton, H.H. II, "Calculation of Laminar Heating Rates on Three-Dimensional Configurations Using the Axisymmetric Analogue," NASA TP 1968, Sept. 1980.

[2] Marconi, F., Yeager, L., and Hamilton, H.H. II, "Computation of High-Speed Inviscid Flows About Real Configurations," *Aerodynamic Analysis Requiring Advanced Computers-Part II*, NASA SP-347, 1975, pp. 1411-1455.

[3] Kutler, P., Reinhardt, W.A., and Warming, R.F., "Multishocked Three-Dimensional Supersonic Flow Fields With Real Gas Effects," *AIAA Journal*, Vol. 11, May 1973, pp. 657-664.

[4] Rizzi, A.W., Klazius, A., and MacCormack, R.W., "A Generalized Hyperbolic Marching Technique for Three-Dimensional Supersonic Flow With Shocks," *Proceedings of the Fourth International Conference on Numerical Methods in Fluid Mechanics*, Lecture Notes in Physics, Volume 35, Robert D. Richtmyer, ed., Springer-Verlag, New York, 1975, pp. 341-346.

[5] Weilmuenster, K.J., and Hamilton, H.H. II, "A Method for Computation of Inviscid Three-Dimensional Flow Over Blunt Bodies Having Large Embedded Subsonic Regions," AIAA Paper 81-1203, June 1981.

[6] Weilmuenster, K.J. and Hamilton, H.H. II, "A Comparison of Computed Space Shuttle Orbiter Surface Pressures With Flight Measurements," AIAA Paper 82-0937, June 1982.

[7] Weilmuenster, K.J. and Hamilton, H.H. II, "High Angles of Attack Inviscid Flow Calculations Over Shuttle Like Vehicles With Comparisons to Experimental Data," NASA TP 2103, May 1983.

[8] Vachris, A.F., and Yeager, L.S., "QUICK-GEOMETRY-A Rapid Response Method for Mathematically Modeling Configuration Geometry," *Applications of Computer Graphics in Engineering*, NASA SP-1390, 1975, pp. 49-73.

[9] Bradley, P.F., Siemers, P.M. III, and Pruett, C.D., "Comparison of Forward Fuselage Space Shuttle Orbiter Flight Pressure Data to Wind-Tunnel and Analytical Results in the Hypersonic Mach Number Range," AIAA Paper 81-2477, Nov. 1981.

[10] Miller, C.G. III, "Measured Pressure Distributions, Aerodynamic Coefficients, and Shock Shapes on Blunt Bodies at Incidence in Hypersonic Air and CF_4," NASA TM 84489, Sept. 1982.

[11] Wells, W.L., "Heating Measurements on Space Shuttle Orbiter Models With Differentially Deflected Elevons," NASA TM 84646, May 1983.